

MATERIALS SCIENCE

High-strength nanocrystalline intermetallics with room temperature deformability enabled by nanometer thick grain boundaries

Ruizhe Su¹, Dajla Neffati², Jaehun Cho¹, Zhongxia Shang¹, Yifan Zhang¹, Jie Ding¹, Qiang Li¹, Sichuang Xue¹, Haiyan Wang¹, Yashashree Kulkarni², Xinghang Zhang^{1*}

Although intermetallics are attractive for their high strength, many of them are often brittle at room temperature, thereby severely limiting their potential as structural materials. Here, we report on a previously unidentified deformable nanocrystalline CoAl intermetallics with Co-rich thick grain boundaries (GBs). In situ micropillar compression studies show that nanocrystalline CoAl with thick GBs exhibits ultrahigh yield strength, exceeding 4.5 gigapascals. Unexpectedly, nanocrystalline CoAl intermetallics also show prominent work hardening to a flow stress of 5.7 gigapascals up to 20% compressive strain. Transmission electron microscopy studies show that deformation induces abundant dislocations inside CoAl grains with thick GBs, which accommodate plastic deformation. Molecular dynamics simulations reveal that the Co-rich thick GBs play a vital role in promoting nucleation of dislocations at the Co/CoAl interfaces, thereby enhancing the plasticity of the intermetallics. This study provides a perspective to promoting the plasticity of intermetallics via the introduction of thick GBs.

INTRODUCTION

B2 ordered intermetallic compounds normally have high strength, high melting point, low density, good thermal conductivity, and excellent oxidation resistance (1–7). However, their extreme brittleness at room temperature limits their applications as practical structural materials. Most B2 intermetallic compounds (CoAl and NiAl) (8–13) are intrinsically brittle due to the lack of independent slip systems. Because of the high antiphase boundary (APB) energy, $\langle 111 \rangle$ type dislocations, which enjoy 12 slip systems, are rarely observed at room temperature. Instead, $\langle 100 \rangle / \{010\}$ slip with only three independent slip systems dominates plastic deformation and does not meet Von Mises criterion. Although FeAl intermetallics deform by activation of $\langle 111 \rangle / \{110\}$ slip systems, they are often brittle at room temperature due to hydrogen embrittlement (14). A new family of materials, IVa–VIII intermetallic compounds, including YAg, YCu, DyCu, and CeAg, are known to sustain a tensile strain of more than 10% at room temperature (15). However, their high-cost and low yield strength, 100 to 200 MPa, make them poor candidates as structural materials.

Extensive studies have been performed to improve the plasticity of B2 intermetallics (NiAl, FeAl, and CoAl) with limited success. Some of the classical approaches for NiAl are briefly summarized below.

1) Grain refinement. Nagpal and Baker (16) showed that room temperature tensile strain improved slightly to 2.5% when the average grain size decreased to 13 μm . The reduction in grain size increases fracture strength more rapidly than yield strength and thus improves tensile ductility.

2) Modifications of grain boundary chemistry. It was shown that L_{12} Ni_3Al single crystals are ductile, whereas polycrystal Ni_3Al is brittle due to poor grain boundary (GB) cohesive strength. The addition of 0.1 weight % B can induce B segregation to the GB, thus improving GB cohesive strength and in turn significantly improving

tensile ductility at room temperatures (17, 18). However, George and Liu (19) showed that modification of GB chemistry with B, C, and Be is ineffective in alleviation of brittle fracture in NiAl.

3) Multiphase composites. Extensive studies have been performed to investigate the influence of second phases, such as metallic phase (20–26), carbides and oxides (27) on deformability of NiAl.

Compared with the well-studied B2 NiAl, CoAl intermetallic, despite its higher strength and comparable melting point, has not drawn much attention due to its worse ductility at room temperature. CoAl alloys reported to date often have tens of micrometers grain size and yield strength less than 2 GPa (28). Some efforts have aimed at improving the ductility of CoAl intermetallics (28). The Co-rich CoAl (such as $\text{Co}_{72}\text{Al}_{28}$) has shown slightly improved compressive strain at room temperature (5). CoAlNiTi alloys with B2 and L_{12} phases appear to have a few percent tensile ductility (2). CoAlC with B2 and E_2 phase also has some tensile ductility at room temperature (1, 3, 29). Although prior studies improved the room temperature plasticity in certain cases, the mechanical strength of CoAl composite decreased markedly to merely a few hundred megapascals at room temperature (29).

Here, we report on an ultrastrong and deformable nanocrystalline CoAl with Co-rich thick grain boundaries. In situ micropillar compression studies inside a scanning electron microscope show that CoAl intermetallic with Co-rich thick GBs has an ultrahigh yield strength of ~ 4.5 GPa and sustains prominent work hardening to a flow stress of ~ 5.7 GPa, one of the highest reported to date among B2 intermetallics. Such a combination of high strength and room temperature compressive deformability rarely exists in intermetallics. Microscopy analyses show high-density $\langle 100 \rangle$ and $\langle 111 \rangle$ type dislocations in CoAl with thick GBs. Molecular dynamics (MD) simulations reveal that the stacking faults (SFs) in Co-rich thick GBs can promote the nucleation of dislocations from the CoAl/Co interfaces and thus enhance the plasticity of CoAl intermetallics. The discovery of thick-GB enabled high strength and plasticity may create new opportunity to design strong and deformable intermetallics for various industrial applications.

Copyright © 2021
The Authors, some
rights reserved;
exclusive licensee
American Association
for the Advancement
of Science. No claim to
original U.S. Government
Works. Distributed
under a Creative
Commons Attribution
NonCommercial
License 4.0 (CC BY-NC).

¹School of Materials Engineering, Purdue University, West Lafayette, IN 47907, USA.

²Department of Mechanical Engineering, University of Houston, Houston, TX 77204, USA.

*Corresponding author. Email: xzhang98@purdue.edu

MATERIALS AND METHODS

Experiments

Multilayers (2- μm -thick Co 4 nm/Al 6 nm and Co 5 nm/Al 5 nm) were sputter-deposited on SiO₂ substrates. The overall atomic composition of the two films was designed to be 50 atomic % (at %) Al, 50 at % Co (Co₅₀Al₅₀) and 60 at % Co, 40 at % Al (Co₆₀Al₄₀), respectively, tailored by adjusting the layer thickness ratio between Al and Co layers. The base pressure of the sputter chamber was 4×10^{-6} Pa, and the deposition rates were 0.35 nm/s for Co and 0.5 nm/s for Al. The two multilayer films were annealed in a high vacuum furnace at 450°C for 1 hour forming nanocrystalline CoAl intermetallics. Bulk CoAl intermetallic with stoichiometric composition was fabricated by arc-melting the mixture of high purity Al (99.9%) and Co (99.9%) under ultrahigh purity argon atmosphere using an Edmund Buhler Arc Melter. X-ray diffraction (XRD) experiments were performed by using a Bruker D8 Discovery X-ray powder diffractometer at room temperature. Transmission electron microscopy (TEM) experiments were performed on a FEI Talos 200X TEM operated at 200 kV. In situ micropillar compression tests were performed by using a Hysitron PI 88xR PicoIndenter inside an FEI Quanta 3D field emission gun (FEG) dual-beam scanning electron microscope (SEM). CoAl pillars with $\sim 1 \mu\text{m}$ in diameter and $\sim 2 \mu\text{m}$ in height were fabricated using the same SEM equipped with focused ion beam.

Simulations

MD simulations of compression were performed on two CoAl nanopillar specimens, one with a regular GB (CoAl) and another with an hexagonal closely packed (HCP) Co layer (CoAl/Co) separating the two grains. The CoAl pillar in B2 structure had a diameter of 12 nm and a height of 24 nm, consisting of two grains of equal thickness oriented along the $[0\bar{1}3]$ and $[013]$ directions, respectively, and separated by a low-energy $\Sigma 5$ GB. The CoAl/Co pillar had a diameter of 13.5 nm and a height of 27 nm, consisting of two grains of equal thickness of 12 nm oriented along the $[0\bar{1}3]$ and $[013]$ directions, respectively. The two grains were separated by a 3-nm-thick HCP Co layer orientated along the $[\bar{1}210]$ direction.

Both pillars were subjected to conjugate gradient energy minimization, followed by equilibration at 300 K for 50 ps. Compression simulation was applied for 900 ps at a constant strain rate of $2 \times 10^8 \text{ s}^{-1}$. All simulations were performed using the Large-scale Atomic/Molecular Massively Parallel Simulator (30), and the results were visualized using Ovito (31). The Al-Co atomic interactions were described by the embedded-atom method potential developed by Pun *et al.* (32).

RESULTS

XRD profiles of the annealed Co 4 nm/Al 6 nm nanolayers are shown in fig. S1A. Various peaks typical for the polycrystalline CoAl

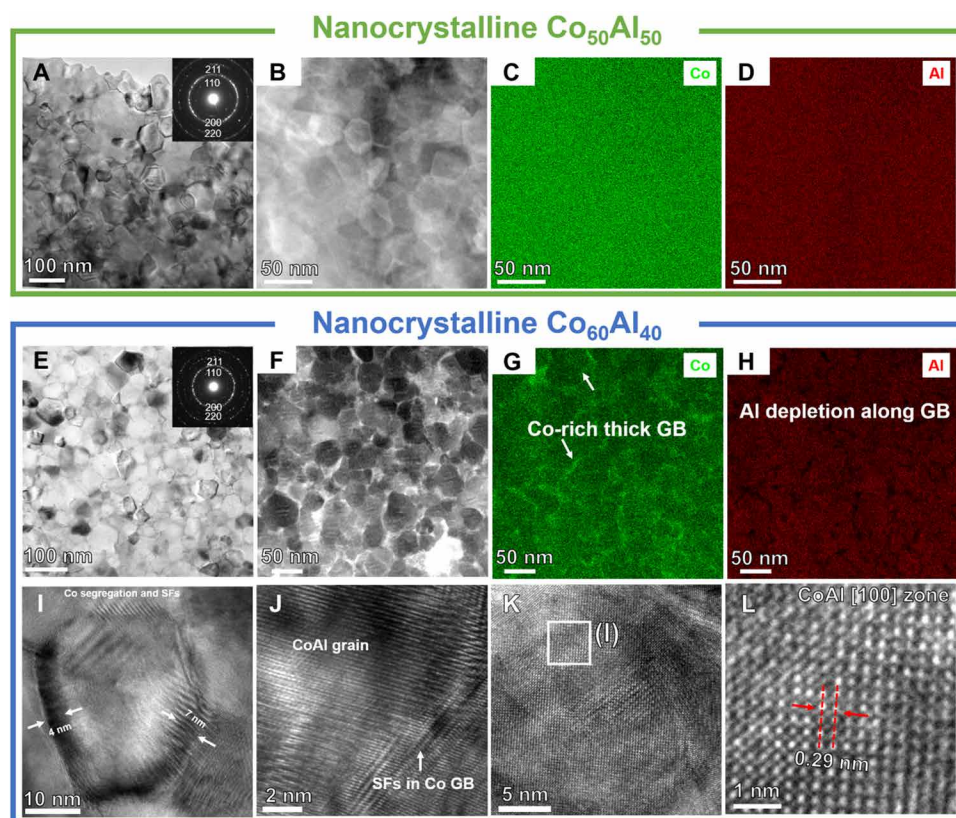


Fig. 1. Microstructures of nanocrystalline Co₅₀Al₅₀ and Co₆₀Al₄₀. (A to D) TEM, STEM micrographs, and EDS maps of nanocrystalline Co₅₀Al₅₀. (A and B) TEM and STEM micrographs show conventional (sharp) grain boundaries between CoAl nanograins. (C and D) EDS maps show homogeneously distributed Al (red) and Co (green) elements. (E to L) TEM, HRTEM, STEM, and EDS maps of nanocrystalline Co₆₀Al₄₀. (E and F) Thicker grain boundaries (2 to 10 nm) were observed in TEM and STEM micrographs. (G and H) EDS maps reveal Co segregation along grain boundaries. (I and J) SFs were observed in the Co-rich phase along grain boundaries. (K and L) HRTEM of CoAl lattice along $[100]$ zone axis. Interplanar spacing measured by HRTEM matches well with literature data for CoAl intermetallics.

intermetallic were observed. Figure 1 shows the TEM micrographs and Energy-dispersive X-ray spectroscopy (EDS) analyses of the nanocrystalline $\text{Co}_{50}\text{Al}_{50}$ and $\text{Co}_{60}\text{Al}_{40}$ derived from the annealing of the nanolayers. Low-magnification and scanning TEM (STEM) micrographs of $\text{Co}_{50}\text{Al}_{50}$ (Fig. 1, A and B) show equiaxed grains with an average grain size of ~ 40 nm. The inserted selected area diffraction pattern confirms the formation of B2 phase. EDS mapping (Fig. 1, C and D) reveals a homogeneous distribution of Co and Al in nanocrystalline $\text{Co}_{50}\text{Al}_{50}$, validating the formation of single-phase CoAl intermetallics. The $\text{Co}_{60}\text{Al}_{40}$ also has nanocrystalline grains with B2 phase (Fig. 1E). However, STEM micrographs (Fig. 1F) show the formation of thick GBs, varying from 2 to 10 nm, with an average GB thickness of ~ 5 nm. EDS maps (Fig. 1, G and H) reveal the segregation of Co in thick GBs. High-resolution TEM (HRTEM) micrographs in Fig. 1 (I and J) show typical CoAl nanograins surrounded by Co-rich thick GBs with SFs, revealed by SFs strips in fast Fourier transform (FFT) on GBs. HRTEM micrographs in Fig. 1 (K and L) confirm the formation of CoAl B2 phase (examined along CoAl $\langle 100 \rangle$ zone axis) within the grains with conventional d-spacing for the intermetallic phase.

The mechanical behaviors of nanocrystalline $\text{Co}_{50}\text{Al}_{50}$ and $\text{Co}_{60}\text{Al}_{40}$ were investigated by nanoindentation (fig. S1B) and in situ SEM micropillar compression tests (Fig. 2). The annealing-induced nanocrystalline $\text{Co}_{50}\text{Al}_{50}$ and $\text{Co}_{60}\text{Al}_{40}$ have high hardness, ~ 15 and 14.6 GPa, respectively, representing one of the hardest intermetallics reported in the literature. In situ compression tests of bulk (casted) single crystal and bicrystal CoAl pillars were also performed for references (Fig. 2 and fig. S2). All pillars have a diameter of 1 to $1.2 \mu\text{m}$ and a height of 2 to $2.5 \mu\text{m}$. Multiple shear bands emerged in the deformed single crystal CoAl (fig. S3), accompanied with intermittent stress-drops on the stress-strain curves. A major shear band was also observed in the deformed bicrystal CoAl. Postdeformation TEM analysis (fig. S4) shows the shear band along the GBs (intergranular crack). Both experiments indicate the brittle nature of CoAl lattice and GBs. Figure 2A compares the true stress-strain curves for nanocrystalline $\text{Co}_{50}\text{Al}_{50}$, $\text{Co}_{60}\text{Al}_{40}$, and bulk bicrystal $\text{Co}_{50}\text{Al}_{50}$ obtained at a constant strain rate ($5 \times 10^{-3}/\text{s}$). Nanocrystalline $\text{Co}_{50}\text{Al}_{50}$ pillars show ultrahigh yield strength, more than 6 GPa, but a crack nucleated at $\sim 11\%$ strain (Fig. 2, D to F), accompanied with a substantial stress drop. Nanocrystalline $\text{Co}_{60}\text{Al}_{40}$ with thick GBs has a yield strength of ~ 4.5 GPa with a prominent work hardening to 5.8 GPa. Instead of forming cracks, the $\text{Co}_{60}\text{Al}_{40}$ exhibited a uniform deformation up to $\sim 20\%$ strain with a slight bulging near the pillar top (Fig. 2, H to J). No shear bands or cracks were observed. See movies S1 and S2 for more details.

Figure 2B compares the fracture stress versus ϵ_{un} (strain where unstable plastic deformation happens, indicated by the formation of shear bands or cracks) for various CoAl, NiAl, and FeAl intermetallics (5, 33–38). Nanocrystalline $\text{Co}_{50}\text{Al}_{50}$ and $\text{Co}_{60}\text{Al}_{40}$ in our study show much higher fracture stress and good deformability compared to prior studies. The ϵ_{un} of nanocrystalline $\text{Co}_{60}\text{Al}_{40}$ reaches an impressive 20%. Figure S5 shows good reproducibility of mechanical tests on $\text{Co}_{50}\text{Al}_{50}$ and $\text{Co}_{60}\text{Al}_{40}$ intermetallic pillars.

DISCUSSION

GBs with a thickness of 1 to 2 nm have been observed in few polycrystalline metallic and ceramic materials, often referred to as GB complexions (39–43). The thickness of GBs reported in our study is

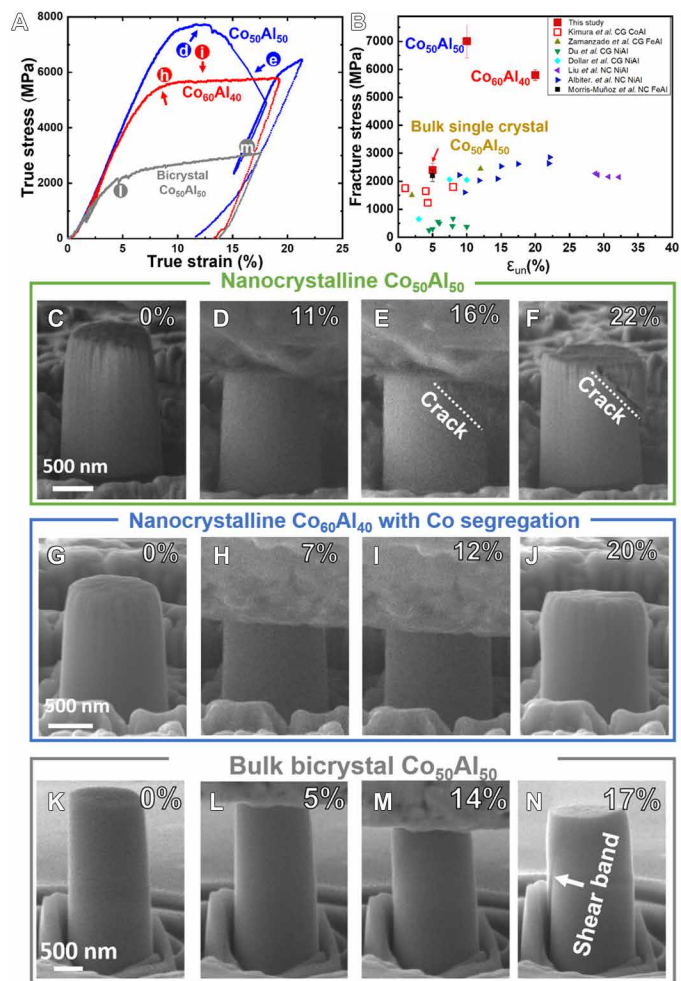


Fig. 2. In situ micropillar compression studies of the three types of CoAl pillars.

(A) True stress-strain curve of nanocrystalline $\text{Co}_{50}\text{Al}_{50}$, $\text{Co}_{60}\text{Al}_{40}$, and bulk bicrystal $\text{Co}_{50}\text{Al}_{50}$ measured by in situ SEM micropillar compression tests. Nanocrystalline $\text{Co}_{50}\text{Al}_{50}$ had the higher strength but a large stress drop was observed at 10 to 15% strain. Nanocrystalline $\text{Co}_{60}\text{Al}_{40}$ had a very high yield strength (4.5 GPa) and work hardened significantly to a flow stress of 5.7 GPa. Bulk bicrystal $\text{Co}_{50}\text{Al}_{50}$ had the flow stress at ~ 2.5 GPa. (B) Comparison of fracture stress and fracture strain between B2 intermetallic alloys (5, 33–38). (C to F) SEM snapshots of nanocrystalline $\text{Co}_{50}\text{Al}_{50}$ show a major shear crack formed during compression, corresponding to the prominent stress drop in the stress-strain curve. (G to J) SEM snapshots of nanocrystalline $\text{Co}_{60}\text{Al}_{40}$ show that the pillar top experienced bulging during plastic deformation, and no cracks or shear bands were observed (see movies S1 and S2 for details). (K to N) SEM snapshots of bulk bicrystal $\text{Co}_{50}\text{Al}_{50}$ show the formation of one single shear band during deformation.

greater than those reported previously. Furthermore, the influence of GB complexion on mechanical behavior of materials is largely unknown. Recently, Ding *et al* (44) reported that Mo segregation leads to thick GBs in Ni-based alloys, and the thick GBs can improve the mechanical strength of Ni alloys because they can effectively block the transmission of dislocations. Furthermore, thick GBs appear to improve the thermal stability of nanocrystalline metals (43, 45). Nanocrystalline MgCu_2 with amorphous shell prepared by magnetron sputtering shows ultrahigh strength (39). But there is little study on

the influence of thick GBs on plasticity of nanocrystalline metals or intermetallics.

Compared with coarse-grained CoAl intermetallics (Fig. 2B) (5, 33–38), grain refinement substantially boosted the yield strength of nanocrystalline $\text{Co}_{50}\text{Al}_{50}$ to more than 6 GPa, but shear bands remain prominent during compression tests (fig. S5). Compared with the compression behaviors of other B2 intermetallics, nanocrystalline $\text{Co}_{60}\text{Al}_{40}$ has an ultrahigh flow stress while still exhibiting a giant uniform compressive strain up to 20% (Fig. 2B). Furthermore, nanocrystalline $\text{Co}_{60}\text{Al}_{40}$ and $\text{Co}_{50}\text{Al}_{50}$ exhibit superior mechanical properties, as illustrated by the Ashby map of specific strength versus specific elastic modulus (fig. S6.). To understand the mechanical properties of nanocrystalline CoAl and reveal the underlying deformation mechanisms of $\text{Co}_{60}\text{Al}_{40}$, systematic post-deformation TEM analyses were performed. A large shear crack was observed in the deformed $\text{Co}_{50}\text{Al}_{50}$ pillar, as revealed by the TEM and STEM micrographs (Fig. 3, A and B). In contrast, no cracks or shear bands were detected in $\text{Co}_{60}\text{Al}_{40}$ pillar deformed to a strain of 20% (Fig. 3E), consistent with the SEM snapshots showing uniform deformation of the pillar (Fig. 2, G to I). High-density SFs are observed inside the Co-rich GB in the deformed $\text{Co}_{60}\text{Al}_{40}$ (Fig. 3F). These SFs may arrive from the migration of Shockley partial dislocations (46–50). The migration of partials in Co-rich thick GBs may carry a small amount of plasticity but cannot explain the 20% giant uniform deformation of the entire $\text{Co}_{60}\text{Al}_{40}$ pillar.

The deformed $\text{Co}_{50}\text{Al}_{50}$ and $\text{Co}_{60}\text{Al}_{40}$ pillars were analyzed by ASTAR automated crystal orientation mapping inside the TEM microscope. Two boxes were selected in the less deformed pillar bottom, defined as region 1, and in the plastically deformed pillar top, defined as region 2. In the deformed $\text{Co}_{50}\text{Al}_{50}$ (Fig. 3, C and D), grains in region 2 (containing a shear crack) were reorientated and elongated along the shear direction (Fig. 3C). Grain size distribution analysis also reveals the grain coarsening (from 40 to 65 nm) in the deformed

area in $\text{Co}_{50}\text{Al}_{50}$ pillar (Fig. 3D). In nanocrystalline materials, dislocation nucleation and pile-ups become increasingly difficult with the reduction of grain sizes (51–53). Correspondingly, GB sliding or grain rotation is frequently observed and dominates the plastic deformation (54–57). In nanocrystalline $\text{Co}_{50}\text{Al}_{50}$, GB sliding and grain reorientation may dominate the plastic deformation. Furthermore, in the shear crack region 2, severely elongated grains due to stress-induced grain coarsening were observed. The aspect ratio of these elongated grains is shown in fig. S7.

In contrast, shear bands or cracks were not observed in the deformed nanocrystalline $\text{Co}_{60}\text{Al}_{40}$ (Fig. 3, E to H). Grains in the largely deformed region 2 in the $\text{Co}_{60}\text{Al}_{40}$ pillar were mostly elongated along the lateral direction, in contrast to the elongation of grains primarily along the shear crack direction in region 2 of the nanocrystalline $\text{Co}_{50}\text{Al}_{50}$ pillar. These observations imply that the plastic deformation in $\text{Co}_{60}\text{Al}_{40}$ is more uniformly accommodated by the deformable CoAl nanograins. So why would the deformability of nanograins be so different in $\text{Co}_{50}\text{Al}_{50}$ and $\text{Co}_{60}\text{Al}_{40}$? To answer this question, systematic HRTEM analyses together with MD simulations were performed.

HRTEM analyses of the deformed grains show prominently different distribution of dislocations in $\text{Co}_{50}\text{Al}_{50}$ and $\text{Co}_{60}\text{Al}_{40}$ samples. To better identify the types of dislocations in deformed grains, we tilted several grains along the [110] zone axis (as shown in Fig. 4 and fig. S8). By using FFT, the filtered HRTEM micrographs in Fig. 4 (B and C) reveal that the deformed $\text{Co}_{50}\text{Al}_{50}$ nanograins contain few scattered [111] type and [100] type dislocations, indicating less dislocation activities and poor intragranular plasticity. However, in the deformed $\text{Co}_{60}\text{Al}_{40}$ grains, the densities of both [111] type and [100] type dislocations are much higher (Fig. 4, E and F). This comparison supports our hypothesis that the intragranular dislocation activities in $\text{Co}_{60}\text{Al}_{40}$ were much more intensive during compression, thus accommodating significant plastic strain. We also compared the

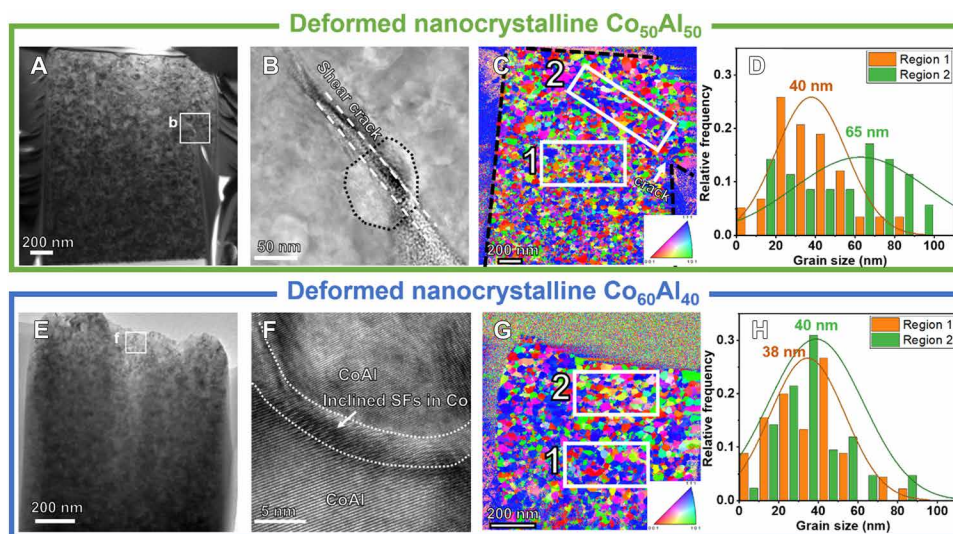


Fig. 3. Post deformation TEM analysis on nanocrystalline $\text{Co}_{50}\text{Al}_{50}$ and $\text{Co}_{60}\text{Al}_{40}$ deformed to ~20% of strain. (A and B) TEM micrographs show a major intragranular shear crack in the deformed nanocrystalline $\text{Co}_{50}\text{Al}_{50}$ pillar. (C) Inverse pole figure (IPF) of the deformed pillar (obtained from ASTAR automated crystal orientation map). A less deformed region 1 and shear band dominated region 2 are outlined in boxes. (D) Statistics shows that the average grain size in region 2 is 65 nm, greater than that in region 1, 40 nm. (E) No shear bands or cracks were observed in the deformed nanocrystalline $\text{Co}_{60}\text{Al}_{40}$ pillar. (F) HRTEM micrograph showing high-density SFs in Co along grain boundaries. (G) IPF of the deformed pillar. Two regions, regions 1 and 2, were selected for further analysis. (H) The average grain sizes in the two regions are similar, ~40 nm. Grains in region 2 elongated slightly after deformation.

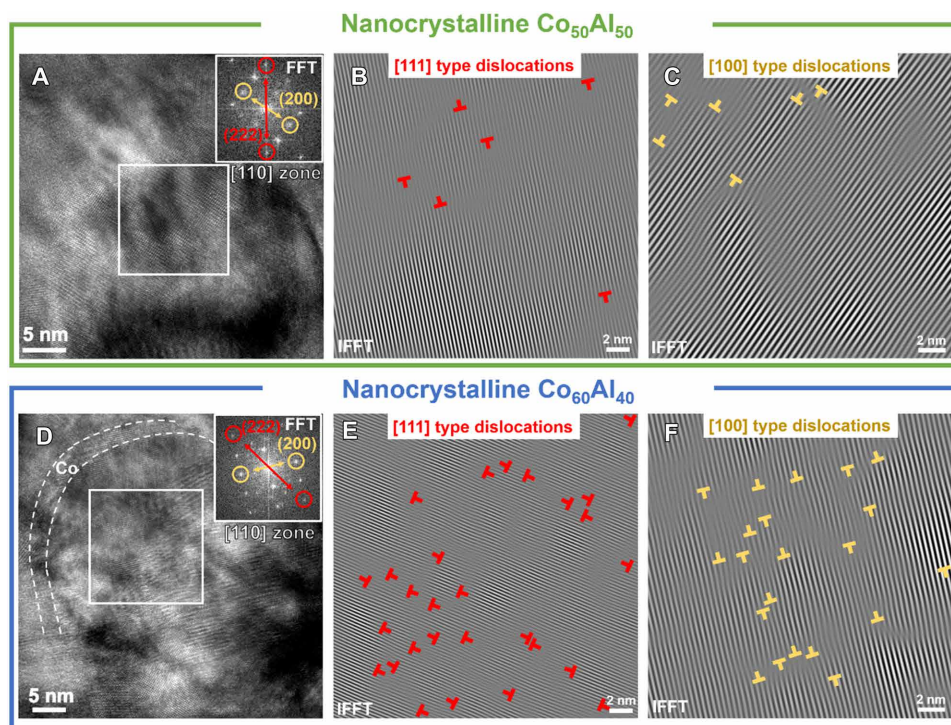


Fig. 4. Dislocations in the deformed nanocrystalline $\text{Co}_{50}\text{Al}_{50}$ and $\text{Co}_{60}\text{Al}_{40}$ pillars. (A) HRTEM micrograph of the deformed nanocrystalline $\text{Co}_{50}\text{Al}_{50}$ showing a grain examined along [110] zone axis. (B and C) Filtered TEM micrographs show few scattered [111] and [100] type of dislocations. (D) HRTEM micrograph of the deformed nanocrystalline $\text{Co}_{60}\text{Al}_{40}$ grain examined along [110] zone axis. (E and F) The inverse fast Fourier transform (IFFT) of the HRTEM micrograph showing high density of [100] and [111] type of dislocations.

dislocation density of $\text{Co}_{60}\text{Al}_{40}$ before and after deformation, as shown in fig. S9. In the deformed $\text{Co}_{60}\text{Al}_{40}$, the densities of both [100] and [111] dislocations are much higher than those in as-annealed $\text{Co}_{60}\text{Al}_{40}$, confirming that high-density dislocations observed in the deformed $\text{Co}_{60}\text{Al}_{40}$ are formed during deformation.

The next question is why are there much more dislocations in the deformed $\text{Co}_{60}\text{Al}_{40}$ pillars than in the $\text{Co}_{50}\text{Al}_{50}$ pillars? Since both samples have equiaxed CoAl grains with similar grain size, we speculate that the drastically different dislocation density is related to the Co-rich thick GBs in the $\text{Co}_{60}\text{Al}_{40}$. Therefore, we performed MD simulations of nanopillar compression to investigate the detailed dislocation nucleation mechanisms in CoAl. Because of the limitation of the spatiotemporal scale of MD simulations, it is computationally prohibitive to mimic the compression of the actual polycrystalline CoAl at experimental size and strain rates. Hence, we focused on identifying deformation mechanisms that can arise from different interfaces. Specifically, we considered two CoAl nanopillars, one with a regular $\Sigma 5$ GB (Fig. 5B), denoted as the CoAl sample, and another with a 3-nm-thick Co layer (mimicking the thick GB observed experimentally), denoted as the CoAl/Co sample (Fig. 5C). MD simulations show that the CoAl pillar with regular GB has a higher yield strength compared with the CoAl/Co pillar (Fig. 5A). Before yielding, no dislocations were observed in the CoAl nanopillar, except for the GB dislocations (Fig. 5D). At the yield point (Fig. 5E), two 45° slip bands nucleated in the upper and lower grains and propagated through the GB, leading to a substantial stress drop (see movie S3 for more details). Consequently, intragranular fracture induced by slip band propagation dominates the plastic deformation (Fig. 5F). The formation of slip bands/cracks is similar to those observed during in situ

micropillar compression tests (Figs. 2F and 3A). Similar mechanical response was also observed in nanopillars with $\Sigma 13$ and $\Sigma 17$ GBs (fig. S10). These simulations suggest that regular GBs in CoAl cannot promote dislocation nucleation, and plasticity is mainly accommodated by shear band propagation.

In contrast, the dislocation activity in the CoAl/Co sample is markedly different. First, high-density inclined SFs were formed in the HCP Co layer (Fig. 5G), in good agreement with our experimental observations (Fig. 3F). Right before yielding, dislocations nucleated at the CoAl/Co interface and aligned along the SF habit planes (Fig. 5, G and H). At the yield point, $\frac{1}{2}[111]$ dislocations (green lines) and [100] dislocations (red lines) nucleated from the CoAl/Co interfaces started to propagate into the CoAl grains (Fig. 5I). During subsequent plastic deformation, instead of forming shear cracks as observed in the CoAl pillar (Figs. 5F and 6A), bulging at the center of the bottom grain in the CoAl/Co pillar became apparent (Fig. 6B), indicating good plasticity under compression. Dislocation analyses show that [100] dislocations nucleated from the CoAl/Co interface propagate downward through the bottom grain (see Fig. 5, J to M, and movie S4 in detail). $\frac{1}{2}[111]$ dislocations cannot propagate over a long distance due to the high APB energy barrier. Instead, they reacted with each other and form [110] and [100] dislocations (see Fig. 5, N to Q, and movie S4 in detail), which can keep gliding across the grain and accommodate plasticity.

When comparing between the deformed CoAl and CoAl/Co nanopillars, an apparent difference is their dislocation densities. A statistical study (Fig. 6) compares the densities and distributions of both [100] and $\frac{1}{2}[111]$ dislocations in the two nanopillars at 13.5% strain (GB dislocations and dislocations in the Co layer are not counted).

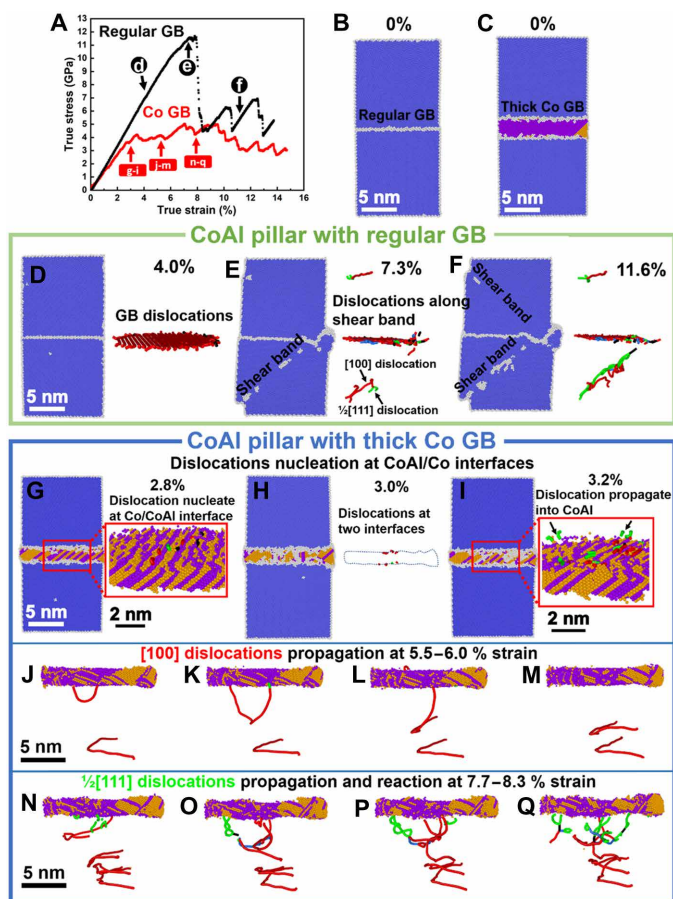


Fig. 5. MD simulations of the CoAl and CoAl/Co nanopillar. (A) True stress-strain curves reveal that CoAl nanopillar has a high flow stress but experiences a sharp stress drop. In comparison, CoAl with Co layer has work hardening without prominent stress drops. (B and C) Initial configuration of CoAl pillars with $\Sigma 5$ GB (B) and thick Co layer (C). Atoms are color coded using common-neighbor analysis, where blue, orange, purple, and white denote Body-centred cubic (BCC), face-centred cubic (FCC), HCP, and unidentified structures, respectively. Green, red, blue, and black lines represent $\frac{1}{2}[111]$ superpartial dislocations, $[100]$, $[110]$, and other dislocations, respectively, identified using dislocation analysis in OVITO. (D to F) Atomic structure (left) and dislocation analysis (right) of CoAl pillar with regular GBs. (D) Dislocations are entangled in regular GB region. (E) Shear band formation leads to the major stress drop shown in Fig. 5A. Dislocations are only observed at the GB and shear band. (F) Plasticity is accommodated by shear band propagation. Few mobile dislocations were observed away from the shear band and GB region. (G and H) Corresponding atomic structure (left) and dislocation analysis (right) of CoAl pillar with thick Co-rich GB. The Co layer contains inclined SFs. (G and H) Right before yielding, dislocations start to nucleate at the CoAl/Co interface along the direction of SFs in Co. (I) $\frac{1}{2}[111]$ dislocations propagate into CoAl grains and lead to yielding. In the CoAl/Co pillar, (J to M) $[100]$ dislocations can propagate through the entire bottom grain. (N to Q) $\frac{1}{2}[111]$ dislocations react with each other to form $[110]$ and $[100]$ dislocations. (See movies S3 and S4 for details).

The total lengths of both types of dislocations in the CoAl/Co sample are much higher than those in the CoAl sample (Fig. 6, C and D), especially the $\frac{1}{2}[111]$ super partial dislocations. It is worth mentioning that the dislocations in the CoAl/Co sample are mobile and homogeneously distributed in the bottom grain, whereas those in the CoAl sample are mostly accumulated along the slip band

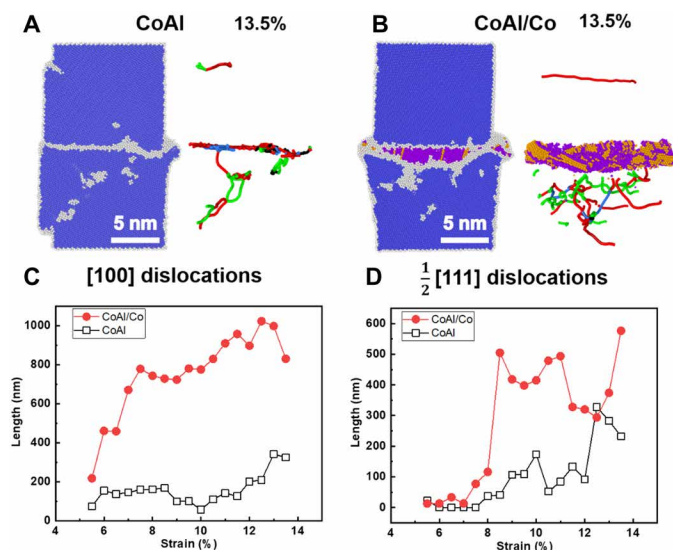


Fig. 6. Dislocation analysis of CoAl pillar and CoAl/Co pillar. (A and B) Atomic structure (left) and dislocation analysis (right) of (A) CoAl pillar and (B) CoAl/Co pillar, respectively, at 13.5% true strain. (C and D) Comparison of total length of (C) $[100]$ and (D) $\frac{1}{2}[111]$ dislocations in the CoAl pillar and the CoAl/Co pillar at different strain. With the existence of the thick Co layer, the densities of both dislocations increase more rapidly than those in the CoAl pillar.

and immobile (similar phenomenon is also observed in CoAl with $\Sigma 13$ and $\Sigma 17$ GBs as shown in fig. S10). Thus, the mobile dislocations that propagated into the grains can accommodate plasticity and prevent brittle shear fracture of the CoAl with Co thick GBs.

The MD simulation results match well with our experimental observations. The ultrafine grain size and high APB energy prohibit the nucleation of dislocations in nanocrystalline stoichiometric $\text{Co}_{50}\text{Al}_{50}$ intermetallics with regular GB. Both experiments and MD simulations show that CoAl samples deform by brittle shear fracture. However, the existence of Co-rich thick GBs (manifested as a Co layer in the MD simulation) can substantially promote the nucleation of dislocations. MD simulation reveals that at the early stage of deformation, dislocations nucleated at the CoAl/Co interface align well with the SFs in Co (Fig. 5G). In general, SFs are bound by two Shockley partial dislocations. Thus, the dislocations in CoAl could originate from the interaction between those Shockley partials and the CoAl/Co interface. There is another possibility that the Shockley partials near the interface increase the local stress, promoting dislocation nucleation. More experiments and simulation studies are needed to understand the role of thick GB and SFs in promoting dislocation nucleation in intermetallics.

We report on an ultrahigh strength, room temperature deformable nanocrystalline CoAl intermetallics ($\text{Co}_{60}\text{Al}_{40}$) with thick GBs fabricated by annealing Al/Co nanolaminates. Nanocrystalline structure and Co-rich thick GBs provide $\text{Co}_{60}\text{Al}_{40}$ with simultaneous high strength and room temperature plasticity, as revealed by in situ SEM compression tests. Postdeformation TEM analyses show that the dislocation density in $\text{Co}_{60}\text{Al}_{40}$ with thick GBs is much greater than that in conventional $\text{Co}_{50}\text{Al}_{50}$. MD simulations elucidate that both $[100]$ and $\frac{1}{2}[111]$ dislocations nucleate from CoAl/Co interface during deformation and propagate through the CoAl grains to accommodate plasticity. Dislocation nucleation at the CoAl/Co interface is

intimately connected to the presence of SFs in the Co-rich thick GBs, an intriguing phenomenon that warrants further investigation. The current study provides a fresh perspective to enhance room temperature plasticity in intermetallics.

SUPPLEMENTARY MATERIALS

Supplementary material for this article is available at <http://advances.sciencemag.org/cgi/content/full/7/27/eabc8288/DC1>

REFERENCES AND NOTES

- Y. Kimura, M. Takahashi, H. Hosoda, S. Miura, Y. Mishima, Compressive mechanical properties of multi-phase alloys based on B2 CoAl and E2₁ Co₃AlC. *Intermetallics* **8**, 749–757 (2000).
- Y. Mishima, M. Kato, Y. Kimura, H. Hosoda, S. Miura, Improvement in room temperature ductility of intermetallic alloys through microstructural control. *Intermetallics* **4**, S171–S179 (1996).
- Y. Kimura, M. Takahashi, S. Miura, Y. Mishima, Phase stability and mechanical properties of multi-phase alloys based on the B2 CoAl and the E2₁ Co₃AlC, in *High-Temperature Ordered Intermetallic Alloys VI, Pts 1 and 2 1995*, J. Horton, I. Baker, S. Hanada, R. D. Noebe, D. S. Schwartz, Eds. (1994), pp. 1371–1376.
- Y. Kimura, S. Miura, T. Suzuki, Y. Mishima, Microstructure and mechanical properties of two-phase alloys based on the B2-type intermetallic compound coal in the Co-Al-Ni ternary system. *Mater. Trans. JIM* **35**, 800–807 (1994).
- Y. Kimura, H. Kuriyama, T. Suzuki, Y. Mishima, Microstructure control and mechanical properties of binary Co-Al alloys based on B2 intermetallic compound CoAl. *Mater. Trans. JIM* **35**, 182–188 (1994).
- Y. Kimura, T. Suzuki, Y. Mishima, Microstructure and mechanical-properties Of B2 (Co, Ni) Al based alloys, in *High-Temperature Ordered Intermetallic Alloys V1993*, I. Baker, R. Darolia, J. D. Whittenberger, M. H. Yoo, Eds. (1992), pp. 697–702.
- E. P. George, M. Yamaguchi, A. K. S. Kumar, C. T. Liu, Ordered Intermetallics. *Annu. Rev. Mater. Sci.* **24**, 409–451 (1994).
- D. L. Yaney, A. R. Pelton, W. D. Nix, Dislocations in extruded Co-49.3at% Al. *J. Mater. Sci.* **21**, 2083–2087 (1986).
- A. G. Rozner, R. J. Wasilewski, Tensile properties of Nial and Niti. *J. Inst. Metals* **94**, 169 (1966).
- K. H. Hahn, K. Vedula, Room temperature tensile ductility in Polycrystalline B2 Nial. *Scrip. Metall.* **23**, 7–12 (1989).
- R. T. Pascoe, C. W. A. Newey, Deformation Modes of the Intermediate Phase Nial. *Phys. Stat. Solidi* **29**, 357–366 (1968).
- R. J. Wasilewski, S. R. Butler, J. E. Hanlon, Plastic deformation of single-crystal Nial. *Trans. Metall. Soc. AIME* **239**, 1357 (1967).
- A. Ball, R. E. Smallman, The operative slip system and general plasticity of NiAl-II. *Acta Metall.* **14**, 1517–1526 (1966).
- C. T. Liu, E. H. Lee, C. G. McKamey, An environmental effect as the major cause for room-temperature embrittlement in FeAl. *Scrip. Metall.* **23**, 875–880 (1989).
- K. Gschneidner Jr., A. Russell, A. Pecharsky, J. Morris, Z. Zhang, T. Lograsso, D. Hsu, C. H. Chester Lo, Y. Ye, A. Slager, D. Kesse, A family of ductile intermetallic compounds. *Nat. Mater.* **2**, 587–591 (2003).
- P. Nagpal, I. Baker, The effect of grain size on the room-temperature ductility of NiAl. *Scrip. Metall. Mater.* **24**, 2381–2384 (1990).
- C. T. Liu, C. L. White, J. A. Horton, Effect of boron on grain-boundaries in Ni3Al. *Acta Metall.* **33**, 213–229 (1985).
- Z. B. Jiao, J. H. Luan, C. T. Liu, Strategies for improving ductility of ordered intermetallics. *Prog. Natural Sci. Mater. Int.* **26**, 1–12 (2016).
- E. P. George, C. T. Liu, Brittle fracture and grain boundary chemistry of microalloyed NiAl. *J. Mater. Res.* **5**, 754–762 (2011).
- J. Shi, Z. H. Cao, M. Z. Wei, G. J. Pan, L. J. Xu, X. K. Meng, Multiple effects of Ni-rich precipitates in Ni-Ti-Al thin films. *Mater. Sci. Eng. A* **623**, 104–108 (2015).
- L. Zhu, C. Wei, H. Qi, L. Jiang, Z. Jin, J.-C. Zhao, Experimental investigation of phase equilibria in the Co-rich part of the Co-Al-X (X = W, Mo, Nb, Ni, Ta) ternary systems using diffusion multiples. *J. Alloys Compd.* **691**, 110–118 (2017).
- J. Yuan, X. Zhang, C. Zhang, K. Sun, C. Liu, In-situ synthesis of NiAl/WC composites by thermal explosion reaction. *Ceram. Int.* **42**, 10992–10996 (2016).
- C.-M. Lin, W.-Y. Kai, C.-Y. Su, K.-H. Key, Empirical alloys-by-design theory calculations to the microstructure evolution mechanical properties of Mo-doped laser cladding NiAl composite coatings on medium carbon steel substrates. *J. Alloys Compd.* **702**, 679–686 (2017).
- A. I. Kovalev, D. L. Wainstein, A. Y. Rashkovskiy, Influence of Al grain boundaries segregations and La-doping on embrittlement of intermetallic NiAl. *Appl. Surf. Sci.* **354**, 323–327 (2015).
- Y. Zhou, F. Zhou, J. M. R. Martins, P. Nash, J. Wang, The effect of discontinuous γ' precipitation on the mechanical properties of Al-Co-Ni alloys. *Mater Charact* **151**, 612–619 (2019).
- P. Lazar, R. Podlucky, Ab initio study of the mechanical properties of NiAl microalloyed by X=Cr,Mo,Ti,Ga. *Phys. Rev. B* **73**, 104114 (2006).
- L. Plazanet, D. Tetard, F. Nardou, Effect of SiC and ZrO₂ particles on the mechanical properties of NiAl. *Compos. Sci. Technol.* **59**, 537–542 (1999).
- B. Nithin, A. Samanta, S. K. Makineni, T. Alam, P. Pandey, A. K. Singh, R. Banerjee, K. Chattopadhyay, Effect of Cr addition on γ - γ' cobalt-based Co-Mo-Al-Ta class of superalloys: A combined experimental and computational study. *J. Mater. Sci.* **52**, 11036–11047 (2017).
- Y. Kimura, Y. Mishima, C. T. Liu, Microstructure control and tensile properties of three-phase alloys based on the E2₁ Co₃AlC and B2 CoAl. *Intermetallics* **9**, 1069–1078 (2001).
- S. Plimpton, Fast parallel algorithms for short-range molecular dynamics. *J. Comput. Phys.* **117**, 1–19 (1995).
- A. Stukowski, Visualization and analysis of atomistic simulation data with OVITO—the Open Visualization Tool. *Modell. Simul. Mater. Sci. Eng.* **18**, 015012 (2010).
- G. P. Pun, Y. Mishin, Embedded-atom potential for hcp and fcc cobalt. *Phys. Rev. B* **86**, 134116 (2012).
- X.-h. Du, C. Gao, B.-I. Wu, Y.-h. Zhao, J.-j. Wang, Enhanced compression ductility of stoichiometric NiAl at room temperature by Y and Cu co-addition. *Int. J. Minerals Metall. Mater.* **19**, 348–353 (2012).
- M. Dollar, S. Dymek, S. J. Hwang, P. Nash, The role of microstructure on strength and ductility of hot-extruded mechanically alloyed NiAl. *Metall. Trans. A* **24**, 1993–2000 (1993).
- E. Liu, J. Jia, Y. Bai, W. Wang, Y. Gao, Study on preparation and mechanical property of nanocrystalline NiAl intermetallic. *Mater. Design* **53**, 596–601 (2014).
- A. Albitser, M. Salazar, E. Bedolla, R. A. L. Drew, R. Perez, Improvement of the mechanical properties in a nanocrystalline NiAl intermetallic alloy with Fe, Ga and Mo additions. *Mater. Sci. Eng. A* **347**, 154–164 (2003).
- M. A. Morris-Muñoz, A. Dodge, D. G. Morris, Structure, strength and toughness of nanocrystalline FeAl. *Nanostruct. Mater.* **11**, 873–885 (1999).
- M. Zamanzade, J. R. Velayarce, O. T. Abad, C. Motz, A. Barnoush, Mechanical behavior of iron aluminides: A comparison of nanoindentation, compression and bending of micropillars. *Mater. Sci. Eng. A* **652**, 370–376 (2016).
- G. Wu, K.-C. Chan, L. Zhu, L. Sun, J. Lu, Dual-phase nanostructuring as a route to high-strength magnesium alloys. *Nature* **545**, 80–83 (2017).
- P. R. Cantwell, M. Tang, S. J. Dillon, J. Luo, G. S. Rohrer, M. P. Harmer, Grain boundary complexions. *Acta Mater.* **62**, 1–48 (2014).
- P. R. Cantwell, T. Frolov, T. J. Rupert, A. R. Krause, C. J. Marvel, G. S. Rohrer, J. M. Rickman, M. P. Harmer, Grain boundary complexion transitions. *Annu. Rev. Mat. Res.* **50**, 465–492 (2020).
- T. J. Rupert, The role of complexions in metallic nano-grain stability and deformation. *Curr. Opin. Solid State Mater. Sci.* **20**, 257–267 (2016).
- A. Khalajhedayat, T. J. Rupert, High-temperature stability and grain boundary complexion formation in a nanocrystalline Cu-Zr Alloy. *JOM* **67**, 2788–2801 (2015).
- J. Ding, D. Neffati, Q. Li, R. Su, J. Li, S. Xue, Z. Shang, Y. Zhang, H. Wang, Y. Kulkarni, X. Zhang, Thick grain boundary induced strengthening in nanocrystalline Ni alloy. *Nanoscale* **11**, 23449–23458 (2019).
- J. Ding, Z. Shang, Y. F. Zhang, R. Su, J. Li, H. Wang, X. Zhang, Tailoring the thermal stability of nanocrystalline Ni alloy by thick grain boundaries. *Scr. Mater.* **182**, 21–26 (2020).
- X. Wu, Y. T. Zhu, M. W. Chen, E. Ma, Twinning and stacking fault formation during tensile deformation of nanocrystalline Ni. *Scr. Mater.* **54**, 1685–1690 (2006).
- R. Su, D. Neffati, J. Cho, Q. Li, J. Ding, H. Wang, Y. Kulkarni, X. Zhang, Phase transformation induced plasticity in high-strength hexagonal close packed Co with stacking faults. *Scr. Mater.* **173**, 32–36 (2019).
- R. Su, D. Neffati, Q. Li, S. Xue, J. Cho, J. Li, J. Ding, Y. Zhang, C. Fan, H. Wang, Y. Kulkarni, X. Zhang, Ultra-high strength and plasticity mediated by partial dislocations and defect networks: Part I: Texture effect. *Acta Mater.* **185**, 181–192 (2020).
- R. Su, D. Neffati, S. Xue, Q. Li, Z. Fan, Y. Liu, H. Wang, Y. Kulkarni, X. Zhang, Deformation mechanisms in FCC Co dominated by high-density stacking faults. *Mater. Sci. Eng. A* **736**, 12–21 (2018).
- Y. Liu, Y. Chen, K. Yu, H. Wang, J. Chen, X. Zhang, Stacking fault and partial dislocation dominated strengthening mechanisms in highly textured Cu/Co multilayers. *Int. J. Plasticity* **49**, 152–163 (2013).
- A. Misra, J. P. Hirth, R. G. Hoagland, Length-scale-dependent deformation mechanisms in incoherent metallic multilayered composites. *Acta Mater.* **53**, 4817–4824 (2005).
- Z. Yuan, I. J. Beyerlein, C. Zhou, Emergence of grain-size effects in nanocrystalline metals from statistical activation of discrete dislocation sources. *Acta Mater.* **90**, 169–181 (2015).

53. V. Sriram, J.-M. Yang, J. Ye, A. M. Minor, Determining the stress required for deformation twinning in nanocrystalline and ultrafine-grained copper. *JOM* **60**, 66–70 (2008).
54. S. Yip, The strongest size. *Nature* **391**, 532–533 (1998).
55. J. R. Weertman, D. Farkas, K. Hemker, H. Kung, M. Mayo, R. Mitra, H. Van Swygenhoven, Structure and mechanical behavior of bulk nanocrystalline materials. *MRS Bull.* **24**, 44–53 (1999).
56. Z. W. Shan, E. A. Stach, J. M. K. Wiezorek, J. A. Knapp, D. M. Follstaedt, S. X. Mao, Grain boundary-mediated plasticity in nanocrystalline nickel. *Science* **305**, 654–657 (2004).
57. C. C. Koch, D. G. Morris, K. Lu, A. Inoue, Ductility of nanostructured materials. *MRS Bull.* **24**, 54–58 (1999).

Acknowledgments

Funding: R.S. and X.Z. acknowledge the financial support by NSF-DMR 1642759. D.N. and Y.K. acknowledge the financial support by NSF-DMR 1508484. Q.L. and S.X. is supported by DOE-OBES under grant no. DE-SC0016337. H.W. acknowledges the support from the U.S. Office of Naval Research (N00014-16-1-2778). Access to the Life Sciences Microscopy Center and Materials Science Microscopy Center at Purdue University are also acknowledged. The support from the Research Computing Data Core at the University of Houston is also

acknowledged. We also acknowledge access to microscopy facilities at DOE Center for Integrated Nanotechnologies. **Author contributions:** R.S. and S.X. fabricated Co/Al multilayers. R.S., Q.L., and J.C. fabricated CoAl pillars and performed the pillar compression test. R.S. prepared TEM samples. Z.S. prepared the bulk CoAl sample and SEM analysis. J.D., Y.Z., Z.S., and S.X. performed the TEM analysis. D.N. and Y.K. performed the MD simulation and the data analysis. X.Z., H.W., and Y.K. designed the project and conducted data analyses and the manuscript preparation. **Competing interests:** All authors declare that they have no competing interests. **Data and materials availability:** All data needed to evaluate the conclusions in the paper are present in the paper and/or the Supplementary Materials. Additional data related to this paper may be requested from the authors.

Submitted 15 May 2020

Accepted 21 May 2021

Published 2 July 2021

10.1126/sciadv.abc8288

Citation: R. Su, D. Neffati, J. Cho, Z. Shang, Y. Zhang, J. Ding, Q. Li, S. Xue, H. Wang, Y. Kulkarni, X. Zhang, High-strength nanocrystalline intermetallics with room temperature deformability enabled by nanometer thick grain boundaries. *Sci. Adv.* **7**, eabc8288 (2021).

High-strength nanocrystalline intermetallics with room temperature deformability enabled by nanometer thick grain boundaries

Ruizhe Su, Dajla Neffati, Jaehun Cho, Zhongxia Shang, Yifan Zhang, Jie Ding, Qiang Li, Sichuang Xue, Haiyan Wang, Yashashree Kulkarni and Xinghang Zhang

Sci Adv 7 (27), eabc8288.
DOI: 10.1126/sciadv.abc8288

ARTICLE TOOLS

<http://advances.sciencemag.org/content/7/27/eabc8288>

SUPPLEMENTARY MATERIALS

<http://advances.sciencemag.org/content/suppl/2021/06/28/7.27.eabc8288.DC1>

REFERENCES

This article cites 55 articles, 1 of which you can access for free
<http://advances.sciencemag.org/content/7/27/eabc8288#BIBL>

PERMISSIONS

<http://www.sciencemag.org/help/reprints-and-permissions>

Use of this article is subject to the [Terms of Service](#)

Science Advances (ISSN 2375-2548) is published by the American Association for the Advancement of Science, 1200 New York Avenue NW, Washington, DC 20005. The title *Science Advances* is a registered trademark of AAAS.

Copyright © 2021 The Authors, some rights reserved; exclusive licensee American Association for the Advancement of Science. No claim to original U.S. Government Works. Distributed under a Creative Commons Attribution NonCommercial License 4.0 (CC BY-NC).